SYSTEMS BIOLOGY

Elucidating the structure and assembly mechanism of actinoporin pores in complex membrane environments

Rocío Arranz[1]†, César Santiago[1]†, Simonas Masiulis[2]†, Esperanza Rivera-de-Torre[3]‡, Juan Palacios-Ortega[3]§, Diego Carlero[1], Diego Heras-Márquez[3], José G. Gavilanes[3], Ernesto Arias-Palomo[4], Álvaro Martínez-del-Pozo[3], Sara García-Linares[3]*, Jaime Martín-Benito[1]*

Pore-forming proteins exemplify the transformative potential of biological molecules. Produced as soluble monomers, they assemble into multimeric membrane-inserted complexes in response to specific membrane environments. Actinoporins, a class of pore-forming proteins from sea anemones, target membranes to kill cells. Here, we report cryogenic electron microscopy structures of two actinoporins, fragaceatoxin C and sticholysin II, reconstituted in lipid membranes. The structures reveal an ordered arrangement of dozens of lipid molecules that form an integral part of the pore architecture. We also captured distinct oligomeric intermediates, arc-shaped assemblies with monomers in transitional conformations, representing key snapshots along the pore formation pathway. These data provide direct structural evidence for a stepwise mechanism in which monomers sequentially bind the membrane and undergo conformational changes that drive pore assembly and membrane disruption. Our findings reveal how these proteins reshape membranes and offer mechanistic insights into their cytolytic activity. This work broadens our understanding of pore-forming proteins, which are gaining increasing relevance in diverse biotechnological applications.

INTRODUCTION

Pore-forming proteins are a rather unique group of metamorphic proteins synthesized as water-soluble monomers that, in contact with the appropriate lipid bilayer, oligomerize and convert into integral membrane proteins to build a pore (*1*). The functions of these proteins vary widely, encompassing, among others, programmed cell death, signaling, immunity, or toxins that attack other cells or organisms. Pore-forming toxins (PFTs) constitute the major class within the pore-forming proteins and have been found in viruses, bacteria, and higher organisms (*2*, *3*). Depending on the secondary structure constituting the transmembrane part of the pore, these toxins are classified either as α- or β-PFTs (*4*–*6*). Among the α-PFTs, actinoporins are recognized as one of the three main constituent families (*2*) and represent one of the most abundant components in the venom of at least 20 species of sea anemones, where they play essential roles in both predation and defense. These proteins constitute multigene families; that is, a single anemone typically expresses several similar genes that produce isoforms with markedly different quantitative pore-forming activities (*7*, *8*). Although the reason for the existence of multiple actinoporin isoforms within a single species remains unclear, we have shown that these isoforms can cooperate to form heteropores with a wide range of cytotoxic potencies (*9*). Moreover, because of their relatively small size (~20 kDa) and the absence of cysteine residues, actinoporins serve as an excellent model for investigating the transition from a water-soluble conformation to a membrane-bound state (*8*). This significance is further underscored by their promising potential in various biotechnological applications (*10*–*13*).

All known actinoporins adopt a well-conserved water-soluble three-dimensional fold (fig. S1). This monomeric structure consists of a β-sandwich, made of 10 to 12 β strands, flanked by two α helices (*14*–*17*). One of the α helices is located at the N-terminal end (α helix 1) and seems to be the only structural element undergoing a notable transformation when the protein binds to the membrane (*18*–*24*). The incorporation of actinoporins into a membrane, and the subsequent formation of a pore, depends largely on the lipid composition and its derived physicochemical properties (*25*–*34*). Sphingomyelin (SM) is specifically required (*28*, *35*–*37*), but other conditions have a strong influence on their pore-forming ability. Some examples of these dependences include the coexistence of various phases or domains, lateral packing, fluidity, membrane thickness, the strength of the interfacial hydrogen bonding network, or the presence of sterols (*22*, *28*, *33*, *38*–*43*). It is well-known that cholesterol (Chol) greatly influences their pore-forming behavior (*30*, *33*, *40*, *41*, *44*–*48*), although the molecular details still remain unknown. Once bound to the membrane, the most generally accepted mechanism of pore formation suggests that α helix 1 extends to the first ~30 residues, and then it is inserted into the membrane to form the pore walls (*17*, *19*–*21*, *43*, *45*, *49*, *50*). This conformational change has to occur in coordination with the oligomerization needed to assemble a stable pore, but the details of this mechanism are far from being understood.

Here, using cryo–electron microscopy (cryo-EM), we have determined the structures of two actinoporins, sticholysin II (StnII) from *Stichodactyla helianthus* (*8*) and fragaceatoxin C (FraC) from *Actinia fragacea* (*51*), within the membrane environment using large unilamelar vesicles (LUVs) and lipid nanodiscs (*52*), both systems

[1]Departamento de Estructura de Macromoléculas, Centro Nacional de Biotecnología, Consejo Superior de Investigaciones Científicas, Calle Darwin 3, 28049 Madrid, Spain. [2]Materials and Structural Analysis Division, Thermo Fisher Scientific, Achtseweg Noord 5, 5651 Eindhoven, Netherlands. [3]Departamento de Bioquímica y Biología Molecular, Universidad Complutense de Madrid, Plaza de las Ciencias 2, 28040 Madrid, Spain. [4]Departamento de Biociencias Celulares y Moleculares, Centro de Investigaciones Biológicas Margarita Salas, Consejo Superior de Investigaciones Científicas, Calle Ramiro de Maeztu 9, 28040 Madrid, Spain.
*Corresponding author. Email: jmartinb@cnb.csic.es (J.M.-B.); sglinares@ucm.es (S.G.-L.)
†These authors contributed equally to this work.
‡Present address: Department of Biotechnology and Biomedicine, Technical University of Denmark, Søltofts Plads 221, DK-2800 Kongens Lyngby, Denmark.
§Present address: Department of Chemistry, Faculty of Natural, Mathematical and Engineering Sciences, King's College London, 7 Trinity Street, SE1 1DB London, UK.

containing 1,2-dioleoyl-*sn*-glycero-3-phosphocholine (DOPC), porcine brain SM, and Chol. In addition, we have isolated and determined the structure of pore intermediates. Our findings prove three key aspects of the pore assembly process. First, lipids play a pivotal role in the final assembly, with SM and Chol forming two well-structured rings containing up to 88 molecules surrounding the pore. Second, while different oligomerization stoichiometries are possible, the octameric arrangement is the most abundant and thermodynamically stable. Last, it is possible to isolate pore-assembling intermediates in lipid nanodiscs. On the basis of these results, we propose a molecular mechanism that outlines the specific sequential events leading to the pore formation, a mechanism that has remained controversial to date (*17*, *50*, *53*).

RESULTS

Structure of the StnII and FraC oligomeric pores on lipid membranes

To elucidate the structure of the FraC and StnII in a membrane environment, we used both liposomes and lipid nanodiscs. The pores were obtained by mixing the water-soluble protein with either LUVs or nanodiscs of the composition DOPC/SM/Chol (80:20:10), as described in Materials and Methods.

Liposome samples revealed that the formed pores tend to cluster in patches when the membrane is not fully covered, leaving certain regions of the vesicle bare (fig. S2A). The pore clusters increase the membrane curvature, producing dome-shaped deformations that protrude from the liposome. At higher toxin concentrations, liposomes are fully covered by pores and exhibit more uniform spherical shapes and reduced diameters, indicating that liposome cleavage may have occurred. On the other hand, the nanodisc preparations are prone to exhibit a preferred orientation on the grid, mostly showing views along the pore longitudinal axis ("top views") and, to a lesser extent, views perpendicular to the longitudinal axis ("side views") (fig. S2B). These behaviors are common to both FraC and StnII proteins.

The structure of FraC in liposomes, resolved at 2.1-Å resolution, reveals an octameric pore with a funnel-shaped arrangement, where the widest part corresponds to the extracellular region when the protein is functioning in its natural environment (Fig. 1 and fig. S3). The structure closely resembles that described by Tanaka *et al.* (*17*), which was determined using detergent-containing crystals and x-ray crystallography [Cα root mean square deviation (RMSD) = 0.388 Å]. However, our data offer an accurate representation of the native lipid organization within the structure, as they were obtained directly for the first time from complex membranes without the use of detergents. The results show that the lipids are arranged in two concentric rings so highly organized that its structure could be solved at high resolution (Fig. 2), indicating that they can be considered a constituent part of the pore (see next section for a detailed description).

The structure of FraC pores resolved in lipid nanodiscs reveals two stoichiometries, a majority one with eight monomers per pore and another, representing ~2% of the total, with a heptameric arrangement (fig. S4A). Although the nanodisc grids containing the pores primarily displayed top views (fig. S2B), the large number of particles in the sample allowed the selection of a final image set with a uniform distribution of views (fig. S4B). The octameric species, solved at 2.5-Å resolution (fig. S4C), exhibits a structure identical to that found in liposomes (fig. S4D). In this case, the electron density corresponding to the lipids surrounding the pore is less well defined than in the LUVs samples, as reflected by the difference in the B factor of the ligands shown in Table 1. This discrepancy may stem from the lower overall resolution of the structure, but it could also result from the proximity of the nanodisc scaffolding protein, which may sterically influence the surrounding lipid molecules, introducing some disturbance in the lipid organization (fig. S5).

The structure of the StnII pores in liposomes was determined at 2.2-Å resolution, revealing a similar arrangement to FraC and confirming the high structural similarity between the two proteins (Cα RMSD = 0.455 Å) (figs. S6 and S7). In the upper part of the transmembrane region, four SM and four Chol molecules per monomer are present, positioned similarly to the FraC pore.

The comparison of the structures of FraC and StnII solved in liposomes reveals a high degree of structural similarity, especially in the topological characteristics of the pore channel and some functionally important amino acids. For instance, tryptophan residues, identified through mutational studies as playing a crucial role in

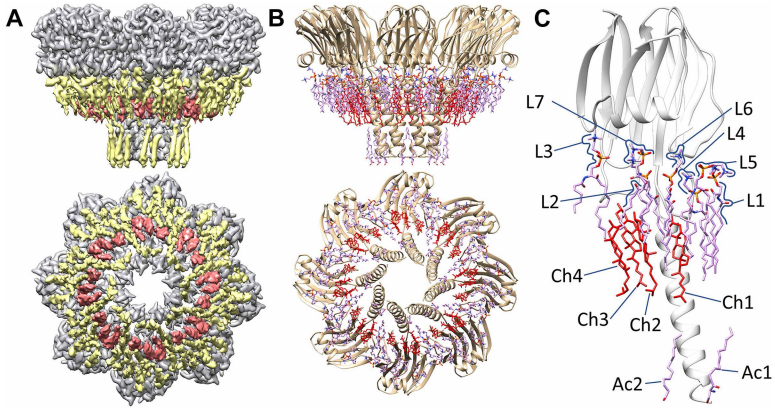

Fig. 1. Atomic structure of FraC pore in the membrane environment. (**A**) Side and bottom views of the cryo-EM map of FraC obtained from LUVs. Densities corresponding to protein, SM, and Chol are shown in gray, yellow, and red, respectively. (**B**) Side and bottom views of the atomic structure of the octamer with the 88 lipid molecules and the 16 acyl chains; SM are colored in pink and Chol in red. (**C**) Lipid arrangement in a monomer. SM molecules are numbered from L1 to L7, Chol from Ch1 to Ch4, and acyl chains Ac1 to Ac2. The FraC monomer has been colored in gray for clarity.

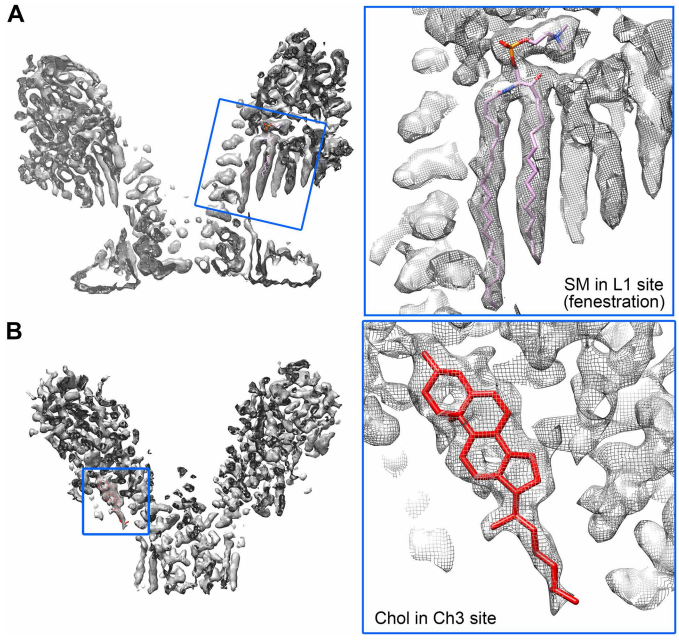

Fig. 2. Lipid densities in FraC pores in LUVs. Two sections of the FraC map showing the density corresponding to the SM present in the fenestration marked as lipid L1 in Fig. 1C (**A**) and the Chol marked as Ch3 in Fig. 1C (**B**).

membrane recognition and pore formation (*32*), exhibit a high spatial coincidence (fig. S8). The most substantial differences arise from the electrostatic potential on the surface of both complexes (Fig. 3). FraC shows negative charges along the entire transmembrane helix of the pore produced by the amino acids Asp^{3}, Asp^{10}, and Asp^{17} and Glu^{24}. In contrast, StnII only has a negative region formed by the amino acids Glu^{22} and Glu^{23} and Asp^{18} clustered in the upper third of the transmembrane helix (Fig. 3A). Moreover, FraC displays a region with distinctly positive character in the β-sandwich connection region to helix 1, contributed by amino acids Lys^{30} and Lys^{32}, Arg^{31} and Arg^{79}, and His^{169}. In comparison, StnII has a smaller positive charge due to the presence of only two amino acids, Lys^{30} and Lys^{168}. Last, another notable difference is found at the exit of the pore on the cytoplasmic side, resulting from the sequence divergence in the first four amino acids at the N-terminal end. The presence of the Asp residue number 3 in FraC, not resolved in the x-ray structure, causes a narrowing at the pore exit and introduces a negative charge absent in the StnII structure, in which this residue is an alanine (Fig. 3B and fig. S9).

Regarding pore stoichiometry, a number of structural and biophysical studies on these PFTs have proposed tetramers (*54*), octamers (*17*), or nonamers (*55*, *56*) as biological complex. In this study, we also demonstrate the presence of heptameric structures in lipid nanodiscs. Recent results (*57*) have led to a consensus that an arrangement of eight subunits is the most thermodynamically stable structure. Accordingly, other stoichiometries would be transient oligomers during pore assembly and have been observed in natural cell membranes (*58*) or model membranes (*17*, *59*, *60*). The results of this study confirm that most of the pores present in the membrane with this lipid composition are octamers, with the heptamer being a structure that, although thermodynamically possible, is likely obtained due to the spatial constrictions imposed by the nanodiscs during the pore formation process.

In summary, our results demonstrate the high similarity between FraC and StnII pores, suggesting that these structural characteristics are likely shared among all sea anemone actinoporins that have the water-soluble structure of a β-sandwich flanked by two α helices (*8*). Consequently, these all proteins would also share a common mechanism in pore formation to exert their cytolytic action.

Role of lipids in pore structure

All structures resolved in this study, whether FraC or StnII, in LUVs or nanodiscs, exhibit a remarkable organization of the lipids around the pore, with nearly identical arrangements in all the cases (Fig. 1 and fig. S10). This finding points out that lipids are not merely the solvating medium of the hydrophobic part of the protein, but rather a constituent part of the pore. Because the structures are essentially identical, we will only describe in detail those obtained in LUVs, as they present higher resolution compared to the structures obtained from nanodiscs.

In the FraC oligomers, a total of 88 lipid molecules can be resolved surrounding the upper part of the transmembrane helix, from which 56 can be attributed to phospholipids, while the remaining 32 were unambiguously identified as Chol molecules (fig. S4). Our data consistently show that SM provides a better fit than DOPC in the phospholipid densities, particularly for the lipid located in the fenestration. For this reason and given the essential role of SM in pore formation, these lipids have been modeled as SM in the atomic structure built into the density maps. However, note that in a natural membrane environment, which contains a diverse array of lipids, some of these positions could potentially be occupied by other structurally similar phospholipids producing a slight change in the pore composition. Eight of the SM molecules occupy the fenestrations between the transmembrane α helices of consecutive monomers, while the other 48 surround the pore forming a wide ring. The Chol molecules are also arranged in a ring around the pore but in the central region of the membrane. The detailed analysis of lipid distribution by monomer reveals that, among the seven SM molecules associated with each monomer (Fig. 1C), the innermost three (named as L1 to L3) match those identified in the crystallographic structure of 4TSY (*17*). These molecules are the ones closely interacting with the protein, including the one located in the fenestration. The remaining four outermost molecules, absent in the crystallographic structure, primarily interact with the protein only through their polar heads (see figs. S10 and S11). The four Chol molecules corresponding to each monomer interact with the hydrophobic part of the transmembrane helix on one side and with the end of the acyl chains of the SMs on the other (see figs. S10 and S11). Furthermore, there are two additional acyl chains per monomer associated to the lower part of the transmembrane region (Fig. 1).

In the case of StnII pores in LUVs, 32 molecules of SM and other 31 molecules of Chol have been resolved in positions completely similar to those of FraC (fig. S10). The fact that in this second case fewer lipids have been built into the density map is most likely due to a slightly lower quality of the density map on the outside of the structure, rather than to real differences in their biochemical behavior.

The close interaction between the lipids and the protein in both cases likely contributes to the high thermodynamic stability exhibited by the protein (*33*, *57*, *61*) (see Discussion). Among these lipids, SM L1 is of special interest because it closes the fenestration

Table 1. Cryo-EM data collection, model refinement, and validation statistics.

	FraC LUVs	FraC nanodiscs	StnII LUVs	StnII pore intermediate (five monomers)	StnII pore intermediate (six monomers)
			Data collection and processing		
EMDB ID	EMD-51426	EMD-51432	EMD-51384	EMD-51420	EMD-51431
Microscope and Ccamera	Titan Krios G4 (E-CFEG) Selectris X Falcon 4i	Titan Krios G3 (X-FEG) Gatan K3	Titan Krios G4 (E-CFEG) Selectris X Falcon 4i	Titan Krios G4 (E-CFEG) Selectris X Falcon 4i	
Voltage (kV)	300	300	300	300	
Magnification	165,000	105,000	165,000	215,000	
Acquisition tilt	0°	0°	0°	30°	
Movies	9088	23,465	14,003	13,427	
Electron dose	52	58	52	45	
Original sampling (Å/pixel)	0.73	1.06	0.73	0.546	
Final processing sampling (Å/pixel)	0.9386	1.06	0.9386	1.093	
Symmetry	C8	C8	C8	C1	
Initial particle images	2.9 M	22.1 M	3.8 M	5.1 M	
Final particle images	282,350	123,451	180,098	272,232	51,975
Resolution (Å) (FSC 0.143)	2.1	2.5	2.2	3.1	4.0
Sphericity in resolution* (out of 1)	0.997	0.998	0.997	0.783	0.723
			Refinement and validation		
PDB ID	9GKL	9GKP	9GJ8	9GKI	9GKO
RMSD lengths (Å)	0.002	0.006	0.007	0.022	0.004
RMSD angles (°)	0.744	0.806	0.968	0.776	0.842
MolProbity score	1.5	1.42	1.57	3.15	2.72
Rotamer outliers(%)	0	0.09	1.81	7.9	0.26
Clash score	9.5	7.7	5.1	31.7	48.8
Ramachandran plot (%)					
Favored	98.6	98.7	97.5	94.6	95.5
Allowed	1.4	1.3	2.53	5.3	4.5
Outliers	0	0	0	0.1	0
B factors (Å^2) min/max/mean					
Protein	33/114/57	46/165/79	9/52/16	82/226/131	131//475/235
Ligand	40/147/92	63/194/136	5/51/30	118/194/147	201/383/254
Composition					
Nonhydrogen atoms	17,520	17,520	12,576	6192	7358
Residues	1424	1424	1400	767	915
Ligands	104	104	56	8	8

*As defined in Aiyer *et al.* (*63*).

gap left between the α helices 1 of adjacent monomers on the extracellular side of the membrane as described (*17*). Our density maps also show how the acyl chains are fully extended to cover the opening between the protomers (Fig. 2 and fig. S7C). On the other hand, the Chol molecules present in both structures are located in the region that approximately corresponds to the hydrophobic core of the membrane, and their positions are rigidly fixed by interaction with the protein and the acyl chains of the SMs. This is an arrangement that fits perfectly with the very well-known preference of Chol for this sphingolipid (*62*). Last, note that the equivalence in lipid positions between FraC and StnII pores further highlights the structural similarity between the two proteins and, presumably, their action mechanisms.

Structure of pore intermediates

Preparations of FraC and StnII on lipid nanodiscs occasionally resulted in intermediate species composed of 4, 5, or 6 monomers, forming half-ring or arc-shaped structures (Fig. 4 and fig. S12A).

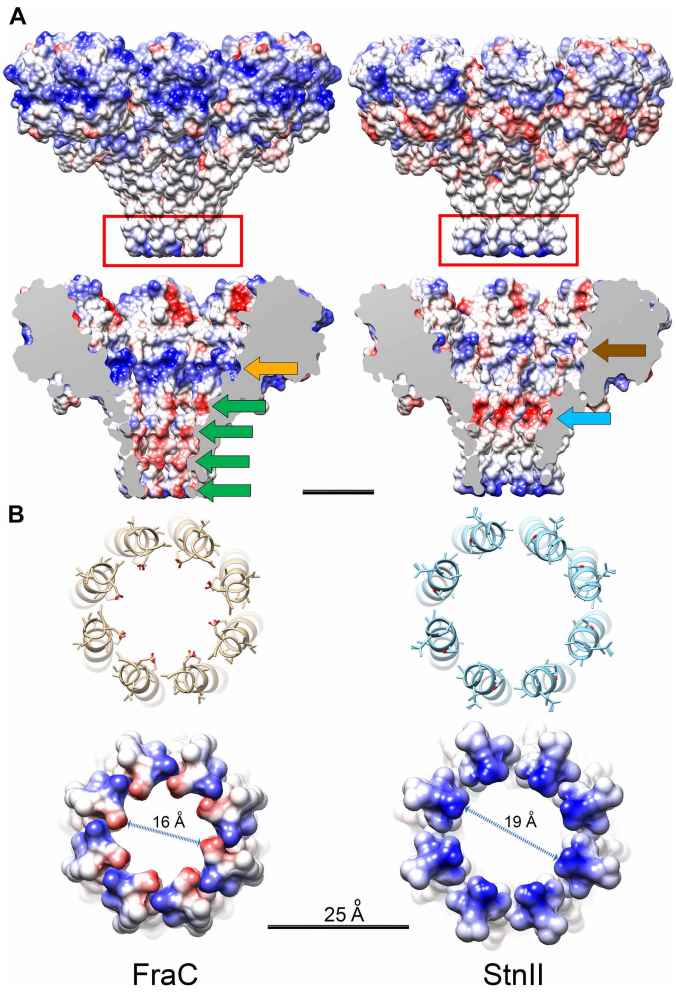

Fig. 3. Comparison of the pore structure of FraC (left) and StnII (right). (**A**) Electrostatic potential of the external surface (top) and inner channel of the pore (bottom). In FraC, the transmembrane helices facing the lumen of the pore are negatively charged along their entire length (green arrows), while StnII exhibits a ring at the top of the helix (blue arrow). In addition, FraC features a ring with an intense positive charge (orange arrow), which is weaker in StnII (brown arrow). (**B**) Detail of the region marked with a red rectangle in (A), corresponding to the lower (cytoplasmic) exit of the pore, which represents the narrowest section in both cases. In FraC, this region has a diameter of ~16 Å and is characterized by a negative charge due to the presence of Asp^3. In contrast, the corresponding region in StnII lacks this charge and has a slightly wider diameter of about 19 Å. Scale bar, 25 Å in both panels.

The two-dimensional (2D) averages revealed a consistent appearance among all the monomers forming the arc, except for the one at one end, which has an additional density facing the center of the pore (Fig. 4A, arrow). The structure of each monomer also resembled that of the monomers in the fully assembled octameric pore, except that the helix inserted in the membrane was not defined in the arcs. All these data suggested that these structures were intermediates of the pore formation process.

To obtain the 3D reconstruction of the pore intermediates in StnII samples, cryo-EM data were taken with a tilt of 30°. This approach was necessary as the nanodiscs exhibit a preferred orientation on the grid, revealing only the top views (fig. S12, A and B). Since the arc structures with five and six monomers were the most abundant, it was possible to attain a 3D reconstruction of these variants at 3.1- and 4-Å resolution, respectively (Fig. 4, B and C), with corresponding resolution anisotropy sphericity values of 0.783 and 0.723, as defined by Aiyer *et al.* (*63*) (Table 1 and fig. S12C). In four monomers, in the case of 5mer arc, and five monomers, for 6mer arc, it is only possible to solve the part corresponding to the β-sandwich and the α helix 2 at the external part of the pore, but the density corresponding to α helix 1 is not defined. In the last monomer, placed at one end of the arc in both cases, it is possible to solve the complete structure and shows a folding similar to that of StnII in its soluble form, with the α helix 1 folded over the β-sandwich (Fig. 4B and fig. S12, D to F). The lateral interaction between the first monomers is virtually the same as that in the complete octameric pore, while the last monomer has a slightly more closed position than would correspond to its equivalent in the complete pore β-sandwich (fig. S12, D and F). Furthermore, the polar headgroups of some lipids, such as those corresponding to L1 and L2 in the complete pore structure, are resolved in contact with the monomers, indicating that these molecules contribute not only to the stabilization of the final pore but also to its assembly (fig. S12E).

In addition, during 2D classification of FraC images in nanodiscs, we obtained an average showing a complete octameric pore, but in which the helices forming the walls of the transmembrane part are not visible (Fig. 4D). While this structure is a minority in the image set (<1%), it could suggest that the disorganization of α helix 1 might persist even when the pore is complete, potentially representing a stage just before membrane piercing for final pore formation. The existence of prepore arrangements such as this was one of the most controversial issues in the field (*50*, *53*).

Note that these pore intermediates were only found in nanodisc samples and not in liposomes. Throughout the entire optimization process for pore sample preparation in LUVs, across multiple experimental conditions, these pore formation intermediates were never observed. One of the reasons that may explain this fact is the limited membrane surface area presented by the nanodiscs to interact with the soluble protein. Consequently, there is a noticeably lower rate of monomer incorporation into the structures that lead to the formation of the final pore, resulting in a slower growth rate, and therefore, the vitrification process can isolate the intermediate structures.

Pore formation mechanism

On the basis of the intermediate pore formation states obtained here and the various atomic structures of StnII, FraC, and other PFTs available, it is possible to propose a detailed pore formation mechanism at the atomic level.

The atomic model built on the StnII pore intermediate structures shows that in four (or five) of its monomers, the α helix 1 is deployed from β-sandwich and extended/disorganized on the membrane surface, while the monomer at the end of the arc keeps this helix folded over the protein main body. The extension of α helix 1 as an initial step in pore formation has also been previously described for the actinoporin equinatoxin II by Rojko *et al.* (*50*). This finding points to a sequential mechanism wherein monomers are incorporated one by one over an initial monomer in the membrane, causing the arc to grow concomitantly with the helix extension process, until it eventually closes into a complete pore. The potential mechanism underlying the simultaneous incorporation of soluble monomers and the unfolding of the helix can be inferred from an examination of the different existing crystallographic structures of PFTs. Comparing these structures,

two noticeable changes in the α helix 1 and in the N-terminal region become apparent: (i) The position of the first about five to seven N-terminal amino acids exhibits high structural variability, presenting two conformations, one proximate to the β-sandwich and the other distanced from it (fig. S13A). (ii) The position of Phe^{14} residue (Phe^{16} in FraC), conserved across most actinoporins (*8*, *48*), also has two main positions, one closely associated with the β-sandwich and the other displaced from its hydrophobic environment (fig. S13B).

Putting all these data together we can outline a mechanism for pore formation (Fig. 5). In the first step, a water-soluble molecule of StnII spontaneously interacts with the membrane surface (*54*) through its well-conserved lipid-binding pockets (*15*, *17*, *37*, *45*). This first membrane-associated monomer serves as a nucleation core for toxin oligomer growth (Fig. 5A). The binding of the next monomer to the membrane, along with the ability to diffuse laterally on the membrane, enables interaction with the first monomer resulting in the formation of a dimer. During this process, the Val^{57} (Val^{60} in FraC) and the N-terminal end of the second monomer can displace Phe^{14} of the first monomer from its hydrophobic environment by steric clash (Fig. 5, B and C), destabilizing the binding of α helix 1 to the β-sandwich and

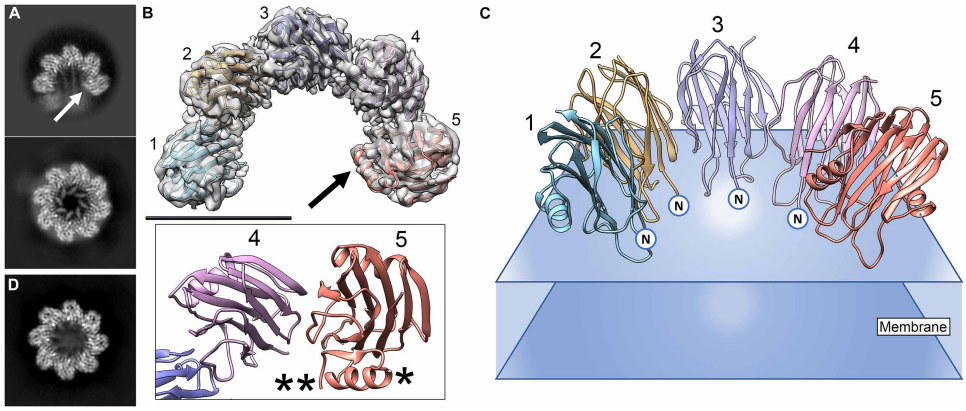

Fig. 4. Structure of pore intermediates. (**A**) 2D average of an intermediate pore composed of five monomers (top) compared with the 2D average of the final octameric pore (bottom). The arrow indicates the distinctive feature of the monomer at the end of the arc. (**B**) Top: Three-dimensional reconstruction and atomic structure built in the pore intermediate of StnII. The arrow points to the α helix 1, which folds over the β-sandwich in the last monomer and corresponds to the distinguishing feature of the 2D average. Scale bar, 50 Å. Bottom: Detail of the atomic structure of monomer 4 and 5 showing the position of the α helix 1 (*) and the N terminus of the last monomer (**). (**C**) Diagram of the atomic structure of the intermediate pore on the membrane (blue planes). The position of the unresolved extended α helix 1 has been marked with an "N" in the first four monomers, while the last monomer [5] is fully resolved. (**D**) Two-dimensional average of an octameric pore in which the helices that form the pore wall are not placed in their final position but remain extended/disordered on the surface of the membrane.

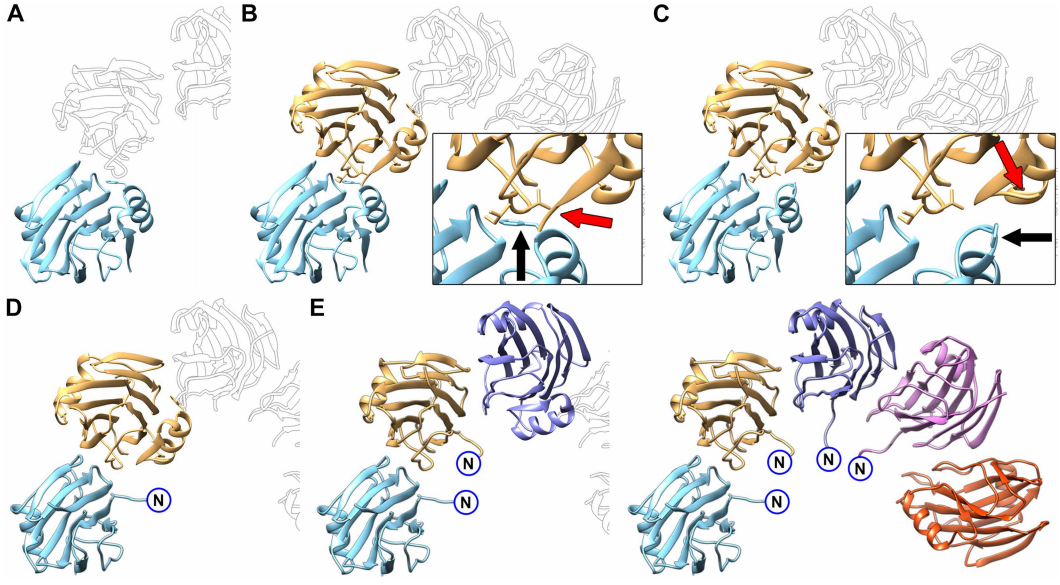

Fig. 5. Pore formation mechanism. (**A**) First monomer (light blue) binds to the membrane. (**B**) Second monomer (brown) laterally interacts and causes a clash between Phe^{14} of the first monomer (black arrow) and Val^{57} and Ile^{58} and N-terminal of the second monomer (red arrow). (**C**) This clash results in displacement of Phe^{14} from its hydrophobic pocket (black arrow) and separation of the N terminus of the second monomer from the β-sandwich (red arrow). (**D**) Displacement of Phe^{14} destabilizes the binding of α helix 1 to the β-sandwich and stretches it over the membrane surface. (**E**) Successive monomer binding drives pore growth. In all panels, the position of monomers in the intermediate pore structure is outlined with black lines.

causing it to unfold over the membrane. A similar effect has been described in FraC crystallographic dimers, with the displacement of the equivalent Phe^{16} by Val^{60} [Protein Data Bank (PDB): 4TSN; fig. S13B] (*48*). This clash also causes the N-terminal end of second monomer to acquire the position separated from the main body of the protein, thus also decreasing its interaction with the β-sandwich. Similarly, the binding of a third monomer will induce the unfolding of the helix of the second monomer, continuing in this manner until the pore is complete (Fig. 5, D to E). Note that biochemical and biophysical data have identified Val^{60} and Phe^{16} in FraC as key residues involved in the formation of the functional pore (*48*). In that study, FraC mutants substituting Phe^{16} exhibited a 1000-fold reduction in hemolytic activity compared to the wild-type protein against sheep erythrocytes; however, they retained the ability to form oligomers in the presence of membranes (*48*). Combining these data with the findings of this study, it is evident that Phe^{16} (Phe^{14} in StnII) directly contributes to the formation of an active pore, specifically in the membrane penetration step, by facilitating the extension of α helix 1. However, it does not play a direct role in the oligomerization process itself.

The determination of the specific moment when membrane perforation occurs cannot be precisely estimated. The images depicting pores with eight monomers, but in which the transmembrane helices are not defined (Fig. 4D), might indicate the presence of a closed structure as the last step before membrane puncturing occurs and suggesting the existence of closed prepores (*53*). On the other hand, studies on liposome-encapsulated substrate release have demonstrated the liberation of large molecules, exceeding the pore diameter, during the assembly process (*61*). This observation suggests that either the process of pore formation, with the appearance of arcs, or the grouping of pores into clusters that deform the vesicles could destabilize the membrane sufficiently to induce partial rupture or excision of liposomes, resulting in leakage of lipid vesicle contents (*61*). In any case, both mechanisms are not mutually exclusive and could potentially coexist during the action of the toxin.

DISCUSSION

In this work, we have determined the structure of two PFTs in the membrane environment using cryo-EM with either LUVs or nanodiscs. Both systems have proven to be good alternatives for resolving the oligomer structure at high resolution, with LUVs yielding better resolution. To the best of our knowledge, this work presents the highest resolution of a membrane protein solved in liposomes to date. Regardless of potential experimental and technical differences in data acquisition for both samples (such as different microscopes, ice conditions, etc.), LUVs offer the advantage that pores are not subject to constrictions caused by the presence of the scaffolding protein in the nanodiscs.

One of the most notable features of the pores is the presence of a large quantity of lipid molecules and their level of organization. The resolution obtained allowed us the identification of individual lipid molecules and to determine that they consist of two rings, one of SM and another of Chol. Unexpectedly, no DOPC molecules were found in the rings, although they constitute a majority of the lipids within the membrane composition used. The presence of a lipid ring surrounding a pore has been shown in other cases by cryo–electron crystallography as in aquaporin-0 (*64*), but it could not be determined what type of lipids formed it because it was a nonspecific interaction. This lipid specificity was not observed in the structure published by Tanaka *et al.* (*17*), probably because of its lower resolution and because the lipids have been replaced by non-natural analogs to facilitate the crystallization process. However, our work shows a structure with two rings of specific composition and formed by a high amount, well-defined lipid molecules. Furthermore, this observation concurs with similar results described for the actinoporin-like Fav pore from the coral *Orbicella faveolata* (*56*).

The general function of lipids bound to the membrane proteins can be divided into three types [reviewed in (*65*)]: (i) specific binding of specific lipids acting as cofactors essential for protein function (*66*); (ii) formation of a lipid ring ("lipid annulus"), different in composition from the bulk of the membrane (*67*), and which is important for the complex functionality (*68*); and (iii) nonselective solvation of the transmembrane domains. In actinoporins it is well established that the presence of SM is essential for their cytolytic action (*25*, *28*–*30*, *35*, *36*, *42*, *45*), whereas Chol enhances efficacy but is not strictly necessary (*40*–*42*, *44*, *46*). The defined position of SMs in the structures solved here suggests that they are an essential component of the pore, such as the one found in the fenestration. However, because SM also forms a ring around the pore, this could be a case where a lipid fits into the first two types of functions mentioned. It should be noted that SM has also been shown to play a key role in membrane recognition by the soluble form of the protein, making the presence of this lipid even more critical.

Regarding Chol, a function could be to accommodate the thickness of the lipid bilayer to the length of the transmembrane fragments of the pore (extended α helix 1). It has been shown that a discrepancy between membrane thickness and length of protein transmembrane regions can lead thermodynamically unfavorable states by potential exposure of hydrophobic zones to the solvent (*69*) and, actually, that seems to be also the case for actinoporins (*43*). On the other hand, PFTs are adapted to act on the plasma membrane, which is thicker (~45 Å) than the inner membranes of the cell (~35 to 40 Å) (*70*). This agrees with the values we obtained by measuring the bilayer thickness in our maps in the area closest to the pore, which are about 41 to 43 Å. In the solved structures, Chol accumulates in the central region of the bilayer, sterically pushing the SM outward and thereby increasing the membrane thickness to better accommodate the helices that form the pore. This hypothesis confers on Chol a role as a thermodynamic stabilizer of the pore once formed, thus confirming biochemical data indicating that it is not an essential component in the toxin action but may enhance its cytolytic performance (*31*, *40*–*42*, *44*, *46*). It is also noteworthy that the composition of the plasma membrane is much richer in Chol (up to 45 mol %) and sphingolipids than those inside the cell, such as the endoplasmic reticulum (down to 5 mol %) indicating the adaptive evolution of these proteins to the plasma membrane.

The stoichiometry of FraC and StnII pores mostly corresponds to octamers, although heptamers were obtained as a minority species (~2%) in some samples prepared on nanodiscs. The presence of these heptamers confirms the ability of these proteins to form structures with different stoichiometries, as demonstrated previously with the crystallographic structure of nonamers in FraC (*55*) and for other PFTs (*71*, *72*). More recently, it has also been demonstrated that the stoichiometry of certain actinoporin-like proteins can depend on the lipid composition (*56*). Nonetheless, it seems probable that the formation of heptameric pores in this case may be favored by constraints imposed by the nanodisc on the pore formation process.

In nanodiscs, arc-shaped structures occasionally appeared, corresponding to pore-forming intermediates. In those intermediates, the monomer at one end retains a structure very similar to the water-soluble form of the protein, while the rest have the α helix 1 deployed over the membrane. On the other hand, early electron microscopy studies on StnII showed its ability to form 2D crystals on lipid monolayers (*15*, *54*). This indicates that the soluble protein can spontaneously bind on the membrane through the described sites (*15*, *17*) and diffuse until it interacts with other monomers. On the basis of these data, we have proposed a mechanism in which a membrane-bound monomer serves as a nucleation point for others to bind by lateral diffusion and form the pore. As described, the mechanism that drives the pore formation is the result of the lateral interaction of the monomers combined with steric clashes, resulting in the extension of the helix on the membrane surface. Last, the timing of the puncture that perforates the membrane is not clear and may occur after the pore closes, as suggested by some microscopy data, or before the structure is complete, as indicated by certain biochemical data on membrane destabilization during pore biogenesis (*61*).

In summary, this study elucidates the structure of two actinoporins within the membrane environment, revealing the involvement of many lipids in the pore arrangement. Furthermore, we propose a mechanism of pore formation that, due to the high structural homology within this family of proteins, is likely common to all its members, advancing our quantitative understanding of the mechanisms underlying pore-forming protein action. From a technical perspective, our findings demonstrate the efficacy of using LUVs decorated with membrane proteins for high-resolution structure determination via cryo-EM. Moreover, we established the utility of nanodiscs in trapping intermediates involved in dynamic processes such as pore formation. All these advances will contribute to a deeper understanding of PFTs and membrane proteins within a broader context, particularly shedding light on the nature of lipid-protein interactions.

MATERIALS AND METHODS

Materials

DOPC, porcine brain SM, and Chol were obtained from Avanti Polar Lipids Inc. (Alabaster, AL, USA). The plasmid used to produce the nanodiscs scaffold protein (MSP1E3D1) was purchased from Addgene (Cambridge, MA, USA).

Protein homogeneity and spectroscopic characterization

The MSP1E3D1 scaffold protein and the actinoporins FraC and StnII were produced and purified as previously described (*13*, *52*, *73*). The homogeneity of protein samples was confirmed by 0.1% SDS and 15% polyacrylamide gel electrophoresis and amino acid analysis, both performed in standard conditions (*16*, *73*, *74*). All protein batches were characterized before use by spectroscopic means, which included recording their near- and far-utraviolet circular dichroism spectra on a Jasco 715 spectropolarimeter (Easton, MD, USA) as described elsewhere (*32*, *33*). Proteins were dissolved at concentrations of 0.2 to 1.0 mg/ml in 15 mM Mops buffer (pH 7.5) containing 100 mM NaCl.

Preparation of LUVs

DOPC/SM/Chol (80:20:10) 100-nm diameter unilamellar vesicles were prepared following standard procedures routinely used in our laboratory (*22*, *33*, *75*). Briefly, an appropriate volume of the lipids dissolved in chloroform/methanol (2:1, v/v) was dried in a UNIVAPO 100H system (Uniequip, Martinsried, Germany) to prepare the lipid vesicles. Then, films were hydrated for 1 hour at 60°C in 20 mM tris-HCl (pH 7.4), containing 100 mM NaCl. The suspension obtained was 15 times extruded through 0.1-μm (pore diameter) Nucleopore filters (Whatman) in a thermobarrel extruder (Lipex Biomembranes, Vancouver, Canada) at 60°C. Vesicles were used immediately after their preparation. Final lipid concentration was estimated from the phosphorous content of the samples (*76*).

Pore assembly within LUVs

Reconstitution of actinoporin pores (FraC or StnII) on LUVs was performed by mixing appropriate amounts of purified actinoporin (prepared in LUV buffer) with liposomes. Several experimental conditions were tested to optimize actinoporin-liposome interactions, including variations in lipid composition, protein to lipid molar ratio, incubation temperature, and interaction time.

The main lipid compositions evaluated were: DOPS/SM/Chol (1:1:1), DOPC/SM (80:20), and DOPC/SM/Chol (80:20:10) (molar ratios). Protein-to-lipid molar ratios of 1:50, 1:100, 1:200, and 1:1000 were assessed. Incubations were carried out at 5°C, room temperature (RT), and 30°C. Notably, incubation at 5°C resulted in significant actinoporin aggregation and poor sample quality. Interaction times ranged from 30 min to 3 hours.

The most consistent and reproducible reconstitution was achieved using DOPC/SM/Chol (80:20:10) at a protein-to-lipid molar ratio of 1:50, with incubation for at least 1 hour at room temperature. These conditions were therefore selected as the standard for subsequent sample preparation.

Nanodiscs reconstitution and purification

Procedure used to reconstitute a homogeneous nanodiscs population was essentially described elsewhere (*13*, *52*) with the particular features of the system employed. These particularities emerged from the inclusion of SM and Chol within the lipid mixtures. Lipid stocks of DOPC/SM/Chol (80:20:10), prepared at 50 mM lipid concentration in chloroform, were used to prepare the convenient lipid dried aliquots. Chloroform was evaporated under a stream of nitrogen. Then, the tubes were placed for 3 hours into a desiccator under high vacuum to remove all traces of the organic solvent. Buffer, containing 200 mM sodium cholate at pH 8.0, was used to rehydrate the lipid film. Typically, cholate was added up to twofold the lipid concentration used. Tubes were then vigorously vortexed, heated at 60°C, and sonicated. Then, the MSP1E3D1 scaffold protein was added to the lipid/detergent mixture to a final protein/lipid ratio of ~1:100 and incubated at room temperature for 15 min. Following, detergent was removed after extensive dialysis against 20 mM tris-HCl (pH 7.4), containing 100 mM NaCl and 0.5 mM EDTA (the chelating agent only during the first dialysis treatment). The final dialyzed solution was centrifuged, and the clear supernatant loaded onto a calibrated Superdex 200 column, equilibrated in the same buffer employed for the dialysis, and attached to an ÄKTA purifier FPLC system (Amersham Biosciences, UK). The resulting chromatogram yielded a symmetrical peak corresponding to the expected molecular size, which was then pooled and labeled as purified empty nanodiscs.

Pore assembly within nanodiscs

Pore assembly was performed with the aim of mimicking the real situation encountered by actinoporins (*13*). Thus, instead of reconstituting

the pore simultaneously with the assembly of the nanodiscs particles, the toxic protein was added to the purified empty nanodiscs preparation at a StnII or FraC/MSP1E3D1 molar ratio of 10:1. This mixture was incubated at room temperature for 1 to 2 hours and then used to prepare the grids used for the cryo-EM analysis. The buffer used was also 20 mM tris-HCl (pH 7.4), containing 100 mM NaCl. The use of the chromatographically purified nanodiscs faction provided the additional advantage that the possible influence of the presence of traces of detergent could be completely ruled out.

Cryo–electron microscopy

Grid preparation and data acquisition of LUVs containing FraC or StnII

Samples obtained as described in the pore assembly within LUVs section were diluted fivefold [to a final concentration of actinoporin (~0.1 mg/ml)] and stained for 1 min with 2% uranyl acetate. The samples were examined using a JEOL 1400 Flash microscope (JEOL, Tokyo, Japan) to verify concentration and quality. A 3 μl of undiluted proteoliposome sample was applied to glow-discharged Quantifoil Cu/Rh R 2/2 Cu 200-mesh grids and blotted away for 3 s and plunge-frozen in liquid ethane. Resulting grids were screened on Talos Arctica microscope (Thermo Fisher Scientific) operated at 200 kV. Selected grids were used for high-resolution imaging on a 300-kV Titan Krios G4 (Thermo Fisher Scientific) instrument equipped with cold field emission electron gun (E-CFEG, Thermo Fisher Scientific), Selectris X energy filter (Thermo Fisher Scientific) and Falcon 4i direct electron detector (Thermo Fisher Scientific) using a pixel size of 0.73 Å/pixel and a total dose of 52 e−/Å^2. A total of 14,002 and 9088 movies in EER file format (*77*) were recorded for StnII and FraC samples, respectively.

Grid preparation and data acquisition of nanodiscs containing FraC or StnII

The concentration of nanodiscs prepared as described above was initially assessed using negative staining. Samples were diluted 10- to 100-fold and screened using negative stain as described in the section above. Dilutions showing a compact and uniform distribution of nanodiscs on the grid surface were selected for cryo-EM analysis. Cryo-EM grids were prepared by depositing 3 μl of the selected concentration onto glow-discharged Quantifoil Cu/Rh R 2/2 grids, followed by vitrification using a Vitrobot Mark IV (Thermo Fisher Scientific). The grid quality was assessed using a Talos Arctica microscope (Thermo Fisher Scientific) operated at 200 kV. The optimal grids were chosen for subsequent data acquisition on a Titan Krios G3i microscope (Thermo Fisher Scientific) at Diamond Light Source (Oxfordshire, UK) using a K3 (Gatan) direct detector. StnII grids displaying higher proportion of half-ring structures were imaged on a 300-kV Titan Krios G4 (Thermo Fisher Scientific) instrument equipped with E-CFEG (Thermo Fisher Scientific), Selectris X energy filter (Thermo Fisher Scientific), and Falcon 4i direct electron detector (Thermo Fisher Scientific). A pixel size of 0.546 Å/pixel and a total dose of 45 e$^-$/Å^2 were used to collect 13,427 movies in EER file format.

Image processing

FraC and StnII pores on LUVs

FraC and StnII pores embedded in LUVs were processed using cryoSPARC (*78*) as summarized in fig. S14. In short, movies were rendered on a 4k × 4k grid, motion corrected and dose-weighted using Patch Motion Correction job type. Next, the contrast transfer function (CTF) parameters were determined using Patch CTF job type. Around 10% of micrographs were removed on the basis of their estimated resolution and drift quality parameters. The selected images were subjected to Topaz (*79*) and template-based particle picking. A 2.9- and 3.8-M particles were picked for FraC and StnII datasets, respectively. Two rounds of 2D classification were performed and 2D classes showing clear actinoporin features were selected. The resulting particle sets underwent multiple rounds of Ab initio, heterogeneous refinement, and 2D classification jobs. This process led to selection of a subset of 282,350 (FraC) and 180,098 particles (StnII), which were both refined to a 2.1- and 2.2-Å resolution EM density maps using non-uniform refinement job type and C8-fold symmetry. In the final reconstruction, per-particle CTF correction implemented in cryoSPARC was applied to refine the CTF values for each micrograph by accounting for local variations.

FraC pores on lipid nanodiscs

All the image processing was carried out inside Scipion3 wrapper (*80*) as summarized in fig. S15. For FraC, 23,465 movies were collected at a calibrated sampling ratio of 1.06 Å/pixel. Frames were aligned using MotionCor2 software (*81*), and CTF was calculated using CTFfind4 (*82*). More than 22.1 million of particles were picked and extracted using Xmipp software (*83*) and 2D classified using cryoSPARC software (*78*). This procedure yielded ~5 million high-quality particles, with ~95% being top views and the rest being side and tilted views. At this point, top views showing C7 symmetry (~2%) were discarded. To avoid overrepresentation of the top views in the spatial sampling during the 3D reconstruction, ~5% of these particles were selected following an image resolution criterion in the different defocus groups of micrographs. All side and tilted views and the selected top views were used for further 3D classification and reconstruction (493,698 particles). The initial model was generated using cryoSPARC (*78*) or Relion4 (*84*, *85*) showing similar results. For 3D classification, the selected particles were rescaled at 1.5 Å/pixel and 128 × 128 pixels and subjected to 3D classification as shown in fig. S15 applying C8 symmetry and using Relion4 software. The particles of the class that showed better resolution (123,451) were selected and re-extracted from original micrographs at 1.06 Å/pixel and 300 × 300 pixels and used for the final reconstruction using cryoSPARC nonuniform refinement procedure (*78*) applying C8 symmetry. In the final reconstruction, per-particle CTF correction implemented in cryoSPARC was applied to refine the CTF values for each micrograph by accounting for local variations.

StnII intermediate pore on lipid nanodiscs

StnII intermediate pore movies as summarized in fig. S16. Briefly, 13,427 movies were motion and CTF-corrected and CTF-curated based on their quality. The resulting 10,085 micrographs were used for template-based particle picking. A total of 5.1 M particles were picked and extensively 2D-classified yielding 429,282 particles, which were further classified using ab initio and heterogeneous refinement job types. The final subsets of 272,232 (5-nucleotide oligomer) and 51,975 (6-nucleotide oligomer) particles were refined to respective 3.1- and 4.0-Å resolutions using C1 symmetry and nonuniform refinement job type. In all cases, per-particle CTF correction protocol implemented in cryoSPARC was applied to account for local tilting effects on the global CTF values. Visualization of structures and figures were created using Chimera software (*86*).

Atomic structures building

A single monomer from FraC atomic structure (PDB: 4TSY) was rigidly fitted into the corresponding density map using Chimera (*86*).

The model was then subjected to a double real-space refinement, initially manually using COOT (*87*), and subsequently using an automatic procedure with PHENIX version 1.21-5207-000 (*88*). The restraints used in the real-space refinement included both standard (bond, angle, planarity, chirality, dihedral, and nonbonded repulsion) and additional restraints (Ramachandran plot, Cβ deviations, rotamer, and secondary structure). A local grid search-based fit was included in the refinement strategy to resolve side-chain outliers (rotamers or poor map regions fitting). Following several rounds of real-space refinement, a stable final model was obtained and validated using the phenix_validation_cryoem module in PHENIX. For Chol and SM, coordinate files were obtained from ChemSpider (www.chemspider.com/; accession numbers 5775 and 24846873, respectively) and loaded into the phenix.elbow program, part of the Phenix suite (v1.20-4559), for restraint and coordinates generation. These ligands were then added to the protein model, positioned within the density, and refined through manual building and real-space fitting using COOT and real-space refinement in Phenix. Last, the octameric model was generated using the Chimera symmetry command and further refined in PHENIX. The same procedure was followed for the complete pore structure of StnII. The half-pore atomic structure for StnII was generated de novo manually, with all molecules in the map constructed and refined in PHENIX.

Supplementary Materials

This PDF file includes:

Figs. S1 to S16

References

REFERENCES AND NOTES

1. J. T. Benton, C. Bayly-Jones, Challenges and approaches to studying pore-forming proteins. *Biochem. Soc. Trans.* **49**, 2749–2765 (2021).
2. M. Dal Peraro, F. G. van der Goot, Pore-forming toxins: Ancient, but never really out of fashion. *Nat. Rev. Microbiol.* **14**, 77–92 (2016).
3. Y. J. Li, Y. L. Li, H. M. Mengist, C. X. Shi, C. Y. Zhang, B. Wang, T. T. Li, Y. Huang, Y. H. Xu, T. C. Jin, Structural basis of the pore-forming toxin/membrane interaction. *Toxins* **13**, 128 (2021).
4. M. W. Parker, S. C. Feil, Pore-forming protein toxins: From structure to function. *Prog. Biophys. Mol. Biol.* **88**, 91–142 (2005).
5. M. Mueller, N. Ban, Enhanced SnapShot: Pore-forming toxins. *Cell* **142**, 334–334.e1 (2010).
6. R. J. C. Gilbert, M. Dalla Serra, C. J. Froelich, M. I. Wallace, G. Anderluh, Membrane pore formation at protein-lipid interfaces. *Trends Biochem. Sci.* **39**, 510–516 (2014).
7. Y. Wang, L. L. Yap, K. L. Chua, H. E. Khoo, A multigene family of *Heteractis* magnificalysins (HMgs). *Toxicon* **51**, 1374–1382 (2008).
8. J. Palacios-Ortega, S. García-Linares, E. Rivera-de-Torre, D. Heras-Márquez, J. G. Gavilanes, J. P. Slotte, A. Martínez-del-Pozo, Structural foundations of sticholysin functionality. *Biochim. Biophys. Acta Proteins Proteom.* **1869**, 140696 (2021).
9. E. Rivera-de-Torre, S. García-Linares, J. Alegre-Cebollada, J. Lacadena, J. G. Gavilanes, A. Martínez-del-Pozo, Synergistic action of actinoporin isoforms from the same sea anemone species assembled into functionally active heteropores. *J. Biol. Chem.* **291**, 14109–14119 (2016).
10. C. Wloka, N. L. Mutter, M. Soskine, G. Maglia, α-Helical fragaceatoxin C nanopore engineered for double-stranded and single-stranded nucleic acid analysis. *Angew. Chem. Int. Ed. Engl.* **55**, 12494–12498 (2016).
11. N. L. Mutter, G. Huang, N. J. van der Heide, F. L. R. Lucas, N. S. Galenkamp, G. Maglia, C. Wloka, Preparation of fragaceatoxin C (FraC) nanopores. *Methods Mol. Biol.* **2186**, 3–10 (2021).
12. C.-W. Ho, V. Van Meervelt, K.-C. Tsai, P. J. De Temmerman, J. Mast, G. Maglia, Engineering a nanopore with co-chaperonin function. *Sci. Adv.* **1**, e1500905 (2015).
13. A. Robles-Martín, R. Amigot-Sánchez, L. Fernandez-Lopez, J. L. Gonzalez-Alfonso, S. Roda, V. Alcolea-Rodriguez, D. Heras-Márquez, D. Almendral, C. Coscolín, F. J. Plou, R. Portela, M. A. Bañares, A. Martínez-del-Pozo, S. García-Linares, M. Ferrer, V. Guallar, Sub-micro- and nano-sized polyethylene terephthalate deconstruction with engineered protein nanopores. *Nat. Catal.* **6**, 1174–1185 (2023).
14. A. Athanasiadis, G. Anderluh, P. Maček, D. Turk, Crystal structure of the soluble form of equinatoxin II, a pore-forming toxin from the sea anemone *Actinia equina*. *Structure* **9**, 341–346 (2001).
15. J. M. Mancheño, J. Martín-Benito, M. Martínez-Ripoll, J. G. Gavilanes, J. A. Hermoso, Crystal and electron microscopy structures of sticholysin II actinoporin reveal insights into the mechanism of membrane pore formation. *Structure* **11**, 1319–1328 (2003).
16. S. García-Linares, I. Castrillo, M. Bruix, M. Menéndez, J. Alegre-Cebollada, A. Martínez-del-Pozo, J. G. Gavilanes, Three-dimensional structure of the actinoporin sticholysin I. Influence of long-distance effects on protein function. *Arch. Biochem. Biophys.* **532**, 39–45 (2013).
17. K. Tanaka, J. M. Caaveiro, K. Morante, J. M. González-Mañas, K. Tsumoto, Structural basis for self-assembly of a cytolytic pore lined by protein and lipid. *Nat. Commun.* **6**, 6337 (2015).
18. G. Anderluh, J. Pungercar, I. Krizaj, B. Strukelj, F. Gubensek, P. Maček, N-terminal truncation mutagenesis of equinatoxin II, a pore-forming protein from the sea anemone *Actinia equina*. *Protein Eng.* **10**, 751–755 (1997).
19. Q. Hong, I. Gutiérrez-Aguirre, A. Barlič, P. Malovrh, K. Kristan, Z. Podlesek, P. Maček, D. Turk, J. M. González-Mañas, J. H. Lakey, G. Anderluh, Two-step membrane binding by equinatoxin ii, a pore-forming toxin from the sea anemone, involves an exposed aromatic cluster and a flexible helix. *J. Biol. Chem.* **277**, 41916–41924 (2002).
20. P. Malovrh, G. Viero, M. D. Serra, Z. Podlesek, J. H. Lakey, P. Maček, G. Menestrina, G. Anderluh, A novel mechanism of pore formation: Membrane penetration by the N-terminal amphipathic region of equinatoxin. *J. Biol. Chem.* **278**, 22678–22685 (2003).
21. K. Kristan, Z. Podlesek, V. Hojnik, I. Gutiérrez-Aguirre, G. Guncar, D. Turk, J. M. González-Mañas, J. H. Lakey, P. Maček, G. Anderluh, Pore formation by equinatoxin, a eukaryotic pore-forming toxin, requires a flexible N-terminal region and a stable β-sandwich. *J. Biol. Chem.* **279**, 46509–46517 (2004).
22. J. Alegre-Cebollada, M. Cunietti, E. Herrero-Galán, J. G. Gavilanes, A. Martínez-del-Pozo, Calorimetric scrutiny of lipid binding by sticholysin II toxin mutants. *J. Mol. Biol.* **382**, 920–930 (2008).
23. U. Ros, W. Rodríguez-Vera, L. Pedrera, P. A. Valiente, S. Cabezas, M. E. Lanio, A. J. García-Saez, C. Álvarez, Differences in activity of actinoporins are related with the hydrophobicity of their N-terminus. *Biochimie* **116**, 70–78 (2015).
24. E. Rivera-de-Torre, J. Palacios-Ortega, S. García-Linares, J. G. Gavilanes, A. Martínez-del-Pozo, One single salt bridge explains the different cytolytic activities shown by actinoporins sticholysin I and II from the venom of *Stichodactyla helianthus*. *Arch. Biochem. Biophys.* **636**, 79–89 (2017).
25. M. L. Shin, D. W. Michaels, M. M. Mayer, Membrane damage by a toxin from the sea anemone *Stoichactis helianthus*. II. Effect of membrane lipid composition in a liposome system. *Biochim. Biophys. Acta* **555**, 79–88 (1979).
26. G. Belmonte, C. Pederzolli, P. Maček, G. Menestrina, Pore formation by the sea anemone cytolysin equinatoxin-II in red blood cells and model lipid membranes. *J. Membr. Biol.* **131**, 11–22 (1993).
27. M. Tejuca, M. D. Serra, M. Ferreras, M. E. Lanio, G. Menestrina, Mechanism of membrane permeabilization by sticholysin I, a cytolysin isolated from the venom of the sea anemone *Stichodactyla helianthus*. *Biochemistry* **35**, 14947–14957 (1996).
28. V. De los Ríos, J. M. Mancheño, M. E. Lanio, M. Oñaderra, J. G. Gavilanes, Mechanism of the leakage induced on lipid model membranes by the hemolytic protein sticholysin II from the sea anemone *Stichodactyla helianthus*. *Eur. J. Biochem.* **252**, 284–289 (1998).
29. C. A. Valcarcel, M. Dalla Serra, C. Potrich, I. Bernhart, M. Tejuca, D. Martínez, F. Pazos, M. E. Lanio, G. Menestrina, Effects of lipid composition on membrane permeabilization by sticholysin I and II, two cytolysins of the sea anemone *Stichodactyla helianthus*. *Biophys. J.* **80**, 2761–2774 (2001).
30. D. Martínez, A. Otero, C. Álvarez, F. Pazos, M. Tejuca, M. E. Lanio, I. Gutiérrez-Aguirre, A. Barlič, I. Iloro, J. L. Arrondo, J. M. González-Mañas, E. Lissi, Effect of sphingomyelin and cholesterol on the interaction of St II with lipidic interfaces. *Toxicon* **49**, 68–81 (2007).
31. B. Bakrač, G. Anderluh, Molecular mechanism of sphingomyelin-specific membrane binding and pore formation by actinoporins. *Adv. Exp. Med. Biol.* **677**, 106–115 (2010).
32. S. García-Linares, T. Maula, E. Rivera-de-Torre, J. G. Gavilanes, J. P. Slotte, A. Martínez-del-Pozo, Role of the tryptophan residues in the specific interaction of the sea anemone *Stichodactyla helianthus*'s actinoporin Sticholysin II with biological membranes. *Biochemistry* **55**, 6406–6420 (2016).
33. S. García-Linares, E. Rivera-de-Torre, K. Morante, K. Tsumoto, J. M. Caaveiro, J. G. Gavilanes, J. P. Slotte, Á. Martínez-del-Pozo, Differential effect of membrane composition on the pore-forming ability of four different sea anemone actinoporins. *Biochemistry* **55**, 6630–6641 (2016).
34. N. Rojko, M. Dalla Serra, P. Maček, G. Anderluh, Pore formation by actinoporins, cytolysins from sea anemones. *Biochim. Biophys. Acta* **1858**, 446–456 (2016).
35. A. W. Bernheimer, L. S. Avigad, Properties of a toxin from the sea anemone *Stoichactis helianthus*, including specific binding to sphingomyelin. *Proc. Natl. Acad. Sci. U.S.A.* **73**, 467–471 (1976).

36. B. Bakrač, I. Gutierrez-Aguirre, Z. Podlesek, A. F. Sonnen, R. J. Gilbert, P. Maček, J. H. Lakey, G. Anderluh, Molecular determinants of sphingomyelin specificity of a eukaryotic pore-forming toxin. *J. Biol. Chem.* **283**, 18665–18677 (2008).
37. T. Maula, Y. J. Isaksson, S. García-Linares, S. Niinivehmas, O. T. Pentikainen, M. Kurita, S. Yamaguchi, T. Yamamoto, S. Katsumura, J. G. Gavilanes, A. Martínez-del-Pozo, J. P. Slotte, 2NH and 3OH are crucial structural requirements in sphingomyelin for sticholysin II binding and pore formation in bilayer membranes. *Biochim. Biophys. Acta* **1828**, 1390–1395 (2013).
38. A. Barlič, I. Gutiérrez-Aguirre, J. M. Caaveiro, A. Cruz, M. B. Ruiz-Argüello, J. Pérez-Gil, J. M. González-Mañas, Lipid phase coexistence favors membrane insertion of equinatoxin-II, a pore-forming toxin from *Actinia equina*. *J. Biol. Chem.* **279**, 34209–34216 (2004).
39. L. Pedrera, M. L. Fanani, U. Ros, M. E. Lanio, B. Maggio, C. Álvarez, Sticholysin I-membrane interaction: An interplay between the presence of sphingomyelin and membrane fluidity. *Biochim. Biophys. Acta* **1838**, 1752–1759 (2014).
40. L. Pedrera, A. B. Gomide, R. E. Sánchez, U. Ros, N. Wilke, F. Pazos, M. E. Lanio, R. Itri, M. L. Fanani, C. Álvarez, The presence of sterols favors sticholysin I-membrane association and pore formation regardless of their ability to form laterally segregated domains. *Langmuir* **31**, 9911–9923 (2015).
41. I. Alm, S. García-Linares, J. G. Gavilanes, Á. Martínez-del-Pozo, J. P. Slotte, Cholesterol stimulates and ceramide inhibits sticholysin II-induced pore formation in complex bilayer membranes. *Biochim. Biophys. Acta* **1848**, 925–931 (2015).
42. J. Palacios-Ortega, S. García-Linares, M. Astrand, M. A. Al Sazzad, J. G. Gavilanes, A. Martínez-del-Pozo, J. P. Slotte, Regulation of sticholysin II-induced pore formation by lipid bilayer composition, phase state, and interfacial properties. *Langmuir* **32**, 3476–3484 (2016).
43. J. Palacios-Ortega, S. García-Linares, E. Rivera-de-Torre, J. G. Gavilanes, A. Martínez-del-Pozo, J. P. Slotte, Differential effect of bilayer thickness on sticholysin activity. *Langmuir* **33**, 11018–11027 (2017).
44. S. García-Linares, I. Alm, T. Maula, J. G. Gavilanes, J. P. Slotte, A. Martínez-del-Pozo, The effect of cholesterol on the long-range network of interactions established among sea anemone Sticholysin II residues at the water-membrane interface. *Mar. Drugs* **13**, 1647–1665 (2015).
45. S. García-Linares, J. Palacios-Ortega, T. Yasuda, M. Astrand, J. G. Gavilanes, A. Martínez-del-Pozo, J. P. Slotte, Toxin-induced pore formation is hindered by intermolecular hydrogen bonding in sphingomyelin bilayers. *Biochim. Biophys. Acta* **1858**, 1189–1195 (2016).
46. J. Palacios-Ortega, S. García-Linares, E. Rivera-de-Torre, J. G. Gavilanes, A. Martínez-del-Pozo, J. P. Slotte, Sticholysin, sphingomyelin, and cholesterol: A closer look at a tripartite interaction. *Biophys. J.* **116**, 2253–2265 (2019).
47. H. P. Wacklin, B. B. Bremec, M. Moulin, N. Rojko, M. Haertlein, T. Forsyth, G. Anderluh, R. S. Norton, Neutron reflection study of the interaction of the eukaryotic pore-forming actinoporin equinatoxin II with lipid membranes reveals intermediate states in pore formation. *Biochim. Biophys. Acta* **1858**, 640–652 (2016).
48. K. Morante, J. M. Caaveiro, K. Tanaka, J. M. González-Mañas, K. Tsumoto, A pore-forming toxin requires a specific residue for its activity in membranes with particular physicochemical properties. *J. Biol. Chem.* **290**, 10850–10861 (2015).
49. I. Gutiérrez-Aguirre, A. Barlič, Z. Podlesek, P. Maček, G. Anderluh, J. M. González-Mañas, Membrane insertion of the N-terminalα-helix of equinatoxin II, a sea anemone cytolytic toxin. *Biochem. J.* **384**, 421–428 (2004).
50. N. Rojko, K. C. Kristan, G. Viero, E. Zerovnik, P. Maček, M. Dalla Serra, G. Anderluh, Membrane damage by an α-helical pore-forming protein, Equinatoxin II, proceeds through a succession of ordered steps. *J. Biol. Chem.* **288**, 23704–23715 (2013).
51. K. Morante, A. Bellomio, A. R. Viguera, J. M. González-Mañas, K. Tsumoto, J. M. M. Caaveiro, The isolation of new pore-forming toxins from the sea anemone *Actinia fragacea* provides insights into the mechanisms of actinoporin evolution. *Toxins* **11**, 401 (2019).
52. T. K. Ritchie, Y. V. Grinkova, T. H. Bayburt, I. G. Denisov, J. K. Zolnerciks, W. M. Atkins, S. G. Sligar, Reconstitution of membrane proteins in phospholipid bilayer nanodiscs. *Methods Enzymol.* **464**, 211–231 (2009).
53. K. Morante, A. Bellomio, D. Gil-Carton, L. Redondo-Morata, J. Sot, S. Scheuring, M. Valle, J. M. Gonzalez-Manas, K. Tsumoto, J. M. M. Caaveiro, Identification of a Membrane-bound Prepore Species Clarifies the Lytic Mechanism of Actinoporins. *J. Biol. Chem.* **291**, 19210–19219 (2016).
54. J. Martín-Benito, F. Gavilanes, V. de Los Ríos, J. M. Mancheño, J. J. Fernández, J. G. Gavilanes, Two-dimensional crystallization on lipid monolayers and three-dimensional structure of sticholysin II, a cytolysin from the sea anemone *Stichodactyla helianthus*. *Biophys. J.* **78**, 3186–3194 (2000).
55. A. E. Mechaly, A. Bellomio, D. Gil-Cartón, K. Morante, M. Valle, J. M. González-Mañas, D. M. A. Guérin, Structural insights into the oligomerization and architecture of eukaryotic membrane pore-forming toxins. *Structure* **19**, 181–191 (2011).
56. G. Solinc, M. Srnko, F. Merzel, A. Crnkovic, M. Kozorog, M. Podobnik, G. Anderluh, Cryo-EM structures of a protein pore reveal a cluster of cholesterol molecules and diverse roles of membrane lipids. *Nat. Commun.* **16**, 2972 (2025).
57. J. Palacios-Ortega, E. Rivera-de-Torre, S. García-Linares, J. G. Gavilanes, A. Martínez-del-Pozo, J. P. Slotte, Oligomerization of Sticholysins from Forster Resonance Energy Transfer. *Biochemistry* **60**, 314–323 (2021).
58. Y. Subburaj, U. Ros, E. Hermann, R. Tong, A. J. García-Sáez, Toxicity of an α-pore-forming toxin depends on the assembly mechanism on the target membrane as revealed by single-molecule imaging. *J. Biol. Chem.* **290**, 4856–4865 (2015).
59. M. A. B. Baker, N. Rojko, B. Cronin, G. Anderluh, M. I. Wallace, Photobleaching Reveals Heterogeneous Stoichiometry for Equinatoxin II Oligomers. *Chembiochem* **15**, 2139–2145 (2014).
60. K. Cosentino, U. Ros, A. J. García-Sáez, Assembling the puzzle: Oligomerization of α-pore forming proteins in membranes. *Biochim. Biophys. Acta* **1858**, 457–466 (2016).
61. J. Palacios-Ortega, E. Rivera-de-Torre, J. G. Gavilanes, J. P. Slotte, A. Martinez-del-Pozo, Evaluation of different approaches used to study membrane permeabilization by actinoporins on model lipid vesicles. *BBA-Biomembranes* **1862**, 183311 (2020).
62. J. P. Slotte, The importance of hydrogen bonding in sphingomyelin's membrane interactions with co-lipids. *Biochim. Biophys. Acta* **1858**, 304–310 (2016).
63. S. Aiyer, C. Zhang, P. R. Baldwin, D. Lyumkis, Evaluating Local and Directional Resolution of Cryo-EM Density Maps. *Methods Mol. Biol.* **2215**, 161–187 (2021).
64. T. Gonen, Y. Cheng, P. Sliz, Y. Hiroaki, Y. Fujiyoshi, S. C. Harrison, T. Walz, Lipid-protein interactions in double-layered two-dimensional AQP0 crystals. *Nature* **438**, 633–638 (2005).
65. I. Levental, E. Lyman, Regulation of membrane protein structure and function by their lipid nano-environment. *Nat. Rev. Mol. Cell Biol.* **24**, 107–122 (2023).
66. S. B. Hansen, X. Tao, R. MacKinnon, Structural basis of PIP2 activation of the classical inward rectifier K+ channel Kir2.2. *Nature* **477**, 495–498 (2011).
67. D. Marsh, Protein modulation of lipids, and vice-versa, in membranes. *Biochim. Biophys. Acta* **1778**, 1545–1575 (2008).
68. M. Murata, J. Peranen, R. Schreiner, F. Wieland, T. V. Kurzchalia, K. Simons, VIP21/caveolin is a cholesterol-binding protein. *Proc. Natl. Acad. Sci. U.S.A.* **92**, 10339–10343 (1995).
69. O. S. Andersen, R. E. Koeppe Ii, Bilayer thickness and membrane protein function: An energetic perspective. *Annu. Rev. Biophys. Biomol. Struct.* **36**, 107–130 (2007).
70. F. A. Heberle, M. Doktorova, H. L. Scott, A. D. Skinkle, M. N. Waxham, I. Levental, Direct label-free imaging of nanodomains in biomimetic and biological membranes by cryogenic electron microscopy. *Proc. Natl. Acad. Sci. U.S.A.* **117**, 19943–19952 (2020).
71. A. F. Kintzer, K. L. Thoren, H. J. Sterling, K. C. Dong, G. K. Feld, I. I. Tang, T. T. Zhang, E. R. Williams, J. M. Berger, B. A. Krantz, The protective antigen component of anthrax toxin forms functional octameric complexes. *J. Mol. Biol.* **392**, 614–629 (2009).
72. M. Mueller, U. Grauschopf, T. Maier, R. Glockshuber, N. Ban, The structure of a cytolytic alpha-helical toxin pore reveals its assembly mechanism. *Nature* **459**, 726–730 (2009).
73. J. Alegre-Cebollada, G. Clementi, M. Cunietti, C. Porres, M. Oñaderra, J. G. Gavilanes, A. Martínez-del-Pozo, Silent mutations at the 5'-end of the cDNA of actinoporins from the sea anemone *Stichodactyla helianthus* allow their heterologous overproduction in *Escherichia coli*. *J. Biotechnol.* **127**, 211–221 (2007).
74. U. K. Laemli, Cleavage of structural proteins during the assembly of the head of bacteriophage T4. *Nature* **227**, 680–685 (1970).
75. J. Palacios-Ortega, E. Rivera-de-Torre, J. G. Gavilanes, J. P. Slotte, A. Martínez-del-Pozo, S. García-Linares, Biophysical approaches to study actinoporin-lipid interactions. *Methods Enzymol.* **649**, 307–339 (2021).
76. G. R. Bartlett, Colorimetric assay methods for free and phosphorylated glyceric acids. *J. Biol. Chem.* **234**, 469–471 (1959).
77. H. Guo, E. Franken, Y. C. Deng, S. Benlekbir, G. S. Lezcano, B. Janssen, L. B. Yu, Z. A. Ripstein, Y. Z. Tan, J. L. Rubinstein, Electron-event representation data enable efficient cryoEM file storage with full preservation of spatial and temporal resolution. *IUCrJ* **7**, 860–869 (2020).
78. A. Punjani, J. L. Rubinstein, D. J. Fleet, M. A. Brubaker, cryoSPARC: Algorithms for rapid unsupervised cryo-EM structure determination. *Nat. Methods* **14**, 290–296 (2017).
79. T. Bepler, A. Morin, M. Rapp, J. Brasch, L. Shapiro, A. J. Noble, B. Berger, Positive-unlabeled convolutional neural networks for particle picking in cryo-electron micrographs. *Nat. Methods* **16**, 1153–1160 (2019).
80. J. M. de la Rosa-Trevín, A. Quintana, L. del Cano, A. Zaldívar, I. Foche, J. Gutiérrez, J. Gómez-Blanco, J. Burguet-Castell, J. Cuenca-Alba, V. Abrishami, J. Vargas, J. Otón, G. Sharov, J. L. Vilas, J. Navas, P. Conesa, M. Kazemi, R. Marabini, C. O. S. Sorzano, J. M. Carazo, Scipion: A software framework toward integration, reproducibility and validation in 3D electron microscopy. *J. Struct. Biol.* **195**, 93–99 (2016).
81. S. Q. Zheng, E. Palovcak, J. P. Armache, K. A. Verba, Y. F. Cheng, D. A. Agard, MotionCor2: Anisotropic correction of beam-induced motion for improved cryo-electron microscopy. *Nat. Methods* **14**, 331–332 (2017).
82. A. Rohou, N. Grigorieff, CTFFIND4: Fast and accurate defocus estimation from electron micrographs. *J. Struct. Biol.* **192**, 216–221 (2015).
83. J. M. de la Rosa-Trevín, J. Otón, R. Marabini, A. Zaldívar, J. Vargas, J. M. Carazo, C. Sorzano, Xmipp 3.0: An improved software suite for image processing in electron microscopy. *J. Struct. Biol.* **184**, 321–328 (2013).

84. D. Kimanius, L. Y. Dong, G. Sharov, T. Nakane, S. H. W. Scheres, New tools for automated cryo-EM single-particle analysis in RELION-4.0. *Biochem. J.* **478**, 4169–4185 (2021).
85. S. H. W. Scheres, RELION: Implementation of a Bayesian approach to cryo-EM structure determination. *J. Struct. Biol.* **180**, 519–530 (2012).
86. E. F. Pettersen, T. D. Goddard, C. C. Huang, G. S. Couch, D. M. Greenblatt, E. C. Meng, T. E. Ferrin, UCSF Chimera—A visualization system for exploratory research and analysis. *J. Comput. Chem.* **25**, 1605–1612 (2004).
87. P. Emsley, B. Lohkamp, W. G. Scott, K. Cowtan, Features and development of Coot. *Acta Crystallogr. D Biol. Crystallogr.* **66**, 486–501 (2010).
88. P. D. Adams, P. V. Afonine, G. Bunkoczi, V. B. Chen, I. W. Davis, N. Echols, J. J. Headd, L. W. Hung, G. J. Kapral, R. W. Grosse-Kunstleve, A. J. McCoy, N. W. Moriarty, R. Oeffner, R. J. Read, D. C. Richardson, J. S. Richardson, T. C. Terwilliger, P. H. Zwart, PHENIX: A comprehensive Python-based system for macromolecular structure solution. *Acta Crystallogr. D Biol. Crystallogr.* **66**, 213–221 (2010).
89. J. L. Vilas, J. Gomez-Blanco, P. Conesa, R. Melero, J. Miguel de la Rosa-Trevin, J. Oton, J. Cuenca, R. Marabini, J. M. Carazo, J. Vargas, C. O. S. Sorzano, MonoRes: Automatic and accurate estimation of local resolution for electron microscopy maps. *Structure* **26**, 337–344.e4 (2018).
90. R. A. Laskowski, M. B. Swindells, LigPlot+: Multiple ligand-protein interaction diagrams for drug discovery. *J. Chem. Inf. Model.* **51**, 2778–2786 (2011).

Acknowledgments: We would like to thank Diamond for access and support of the cryo-EM facilities at the UK National Electron Bio-Imaging Centre (eBIC), proposals BI22006 and BI30374. To Instruct-ERIC for facilitate access for cryo-EM screening through the project PID-18916 and to the cryo-EM facility of the Centro Nacional de Biotecnología in Madrid (CNB-CSIC). CNB-CSIC acknowledges support from the Severo Ochoa Program for Centers of Excellence in R&D (CEX2023-001386-S). **Funding:** This work was supported by grants PID2020-117752RB-I00 and PID2024-162190OB-I00 financed by MCIU/AEI/10.13039/501100011033 from Spanish Ministerio de Ciencia, Innovación y Universidades and FEDER, UE and grant TED2021-132748B-I00 financed by the European Union "NextGeneration EU"/PRTR (to J.M.-B.); the UCM-Banco Santander Grants PR87/19-22556 and PR108/20-26896 and UnaEuropa (Unano) SF2106 (to A.M-.d-.P.). the UCM-Banco Santander Grant PR3/23-30816 (to S.G.-L.); and the Grant PID2022-140651NB-I00 from Spanish Ministerio de Ciencia, Innovación y Universidades (to C.S.). E.R.-d.-T. is supported by a UCM-Banco Santander PhD fellowship grant and the European Research Council (ERC) under the European Union's Horizon 2020 research and innovation program (850974). J.P.-O. is recipient of a doctoral fellowship from ISB and a postdoctoral grant from the Magnus Ehrnrooth Foundation. D.H.-M. thanks Complutense University of Madrid and Banco Santander for a PhD fellowship (CT82/20-CT83/20). **Author contributions:** Experiments were designed and conceived by R.A., C.S., S.M., J.G.G., A.M.d.-P., S.G.-L., and J.M.-B. Protein production and purification and pore preparation experiments were performed by E.R.d.-T., D.H.-M., and S.G.-L. MSP for nanodiscs was prepared by E.R.d.-T. and S.G.L. Cryo-EM structural experiments and analyses were performed by R.A., C.S., S.M., J.P.-O., D.C., E.A.-P., and J.M.B. J.G.G., A.M.-d.-P., S.G.-L., and J.M.-B. supervised the work. A.M.-d.-P., S.G.-L., and J.M.-B. wrote the manuscript. All authors contributed to editing the manuscript, discussing the results and supporting its conclusions. **Competing interests:** The authors declare that they have no competing interests. **Data and materials availability:** All data needed to evaluate the conclusions in the paper are present in the paper and the Supplementary Materials. Cryo-EM maps and atomic coordinates have been deposited in the Electron Microscopy Data Bank (www.ebi.ac.uk/emdb/) and the Protein Data Bank (www.rcsb.org/) under the following accession codes: EMD-51426 and PDB: 9GKL for FraC in LUVs, EMD-51432 and PDB: 9GKP for FraC in nanodiscs, EMD-51384 and PDB 9GJ8 for StnII in LUVs, EMD-51420 and PDB: 9GKI for the five-monomer StnII prepore, and EMDB-51431 and PDB: 9GKO for the six-monomer StnII prepore.

Submitted 6 December 2024
Accepted 25 August 2025
Published 24 September 2025
10.1126/sciadv.adv0683